APPLIED SCIENCES AND ENGINEERING

Pressure-driven microinjection (PMI) of porous-coated balloon for ultrafast endoluminal drug delivery across biological barriers

Honglin Qian[1,2,3]†, Jing Wang[1,3]*†, Zhaohe Dai[4]†, Yirong Guo[2], Ke Liu[1,4], Xinyi Li[2], Meng Hu[2], Yan Yu[2], Jiarong Wang[2], Yuxian Lai[2], Kefeng Ren[2], Jian Ji[1,2,3]*

Biological barriers play a crucial role in safeguarding the human body against pathogens yet pose severe challenges to efficient delivery of therapeutic drugs. Here, we introduce a pressure-driven microinjection (PMI) strategy for the robust and versatile delivery of functional species against biological barriers. With the benefits of elastic porous coating, this strategy enables the capillary suction of drug solutions, localized delivery, and ultrafast penetration through biological barriers by gentle pressure treatment. The penetration capacity is demonstrated by an unprecedented depth (~150 micrometers) of bovine serum albumin (66.4 kilodaltons) across aortic vessels under pressing for only 60 seconds. This spongy coating-based PMI technique can be integrated with medical balloon devices, offering endoluminal treatment within blood vessels, tracheas, and intestines. The in vivo evaluation indicated efficient trans-vascular delivery of 4-octyl itaconate, markedly reducing neointima hyperplasia. This PMI strategy provides a crucial insight for penetrative drug delivery across complex biological barriers.

INTRODUCTION

The human body has developed elaborate and efficient biological barriers within the lumen system to ward off the intrusion of pathogens, including bacteria, viruses, fungi, and harmful chemicals (*1*, *2*). Typical biological barriers comprise three distinct layers: a basement membrane network underlying at the base, a tightly conjunct cell layer in the middle, and a dense glycosaminoglycan network extending from the cells. These structures are found all over the body, such as air-blood barrier in the lungs (*3*, *4*), endothelial barrier in blood vessels (*5*–*8*), and mucus barrier in various organs (*9*–*13*), which are crucial for repelling the intruders and maintaining the homeostasis within the tissues. However, this protective mechanism can also hinder drug delivery systems within their respective organs. Typically, the endothelium barriers, composed of tight junctions and dense basement membranes, only have tiny openings of nanometers in size, impeding the delivery of drugs into brain tissue (*5*–*8*). Thus, the design of materials traversing the barriers has attracted tremendous research interest. Nanomedicines with specialized size, zeta potential, and surface chemistry have been developed to enhance the transport of therapeutics across biological barriers (*14*–*19*). Surface charge regulation could improve nanoparticle penetration by modifying zwitterionic polymers (*20*) or cationic fluorinated polyether imide (*21*). In addition, particles modified with target ligands can further improve the delivery across specific obstacles (*22*–*25*). However, long-term transportation in circulation system markedly hinders accumulation at lesion sites. Besides, the delivery of nanomedicines was mainly concentration-dependent passive diffusion, while the active penetration was specifically designed for the transport to target cells (*26*–*28*). Therefore, developing an efficient and straightforward method to overcome various biological barriers is a pressing challenge for disease treatment.

Compared to the systematic circulation and passive diffusion strategy of nanomedicines, physical techniques, such as microneedles (*29*), needleless injection (*30*, *31*), sonophoresis (*32*, *33*), iontophoresis (*34*), and electroporation (*35*), offer a localized and straightforward approach to overcoming biological barriers through active physical stimulation. For example, microneedles enable diversified drug delivery across cuticle barriers via the puncture of micrometer-sized needles (*29*, *36*, *37*). Iontophoresis, on the other hand, can enhance drug penetration in a noninvasive manner by the implantation of electrodes. Despite the substantial efforts invested in advanced physical techniques, their in vivo administration remains risky due to the damage to the tissue and residual foreign materials (*38*–*40*). In general, an ideal and versatile barrier penetration strategy faces several challenges: (i) effective accumulation of drugs at the target site while minimizing loss during delivery; (ii) rapid, robust, and minimally invasive penetration process; and (iii) with the capacity of combining with medical devices. Recent developments in microneedle systems have incorporated interventional balloons for drug delivery into blood vessels during dilation (*41*). However, the large size (10 to 100 μm) of the microneedles and the introduction of long-term implants can lead to severe vascular endothelium injury and impede blood vessel regeneration. There remains an unmet need to develop a noninvasive and efficient strategy for endoluminal drug delivery across complex biological barriers.

Here, we report a pressure-driven microinjection (PMI) platform using compressible porous coating for ultrafast, localized, and minimally invasive drug delivery across biological barriers. Porous materials have been extensively investigated in drug delivery for medical devices, such as cardiovascular stents (*42*–*45*) and orthopedic implants (*46*, *47*). The spongy coating can serve as a protective reservoir for drug solutions due to the wicking effect and restricted

[1]State Key Laboratory of Transvascular Implantation Devices, The Second Affiliated Hospital Zhejiang University School of Medicine, Xiaoshan District, Hangzhou, 311200, China. [2]MOE Key Laboratory of Macromolecular Synthesis and Functionalization, Department of Polymer Science and Engineering, Zhejiang University, Xihu District, Hangzhou, 310058, China. [3]Transvascular Implantation Devices Research Institute, Binjiang District, Hangzhou, 310051, China. [4]Department of Advanced Manufacturing and Robotics, Peking University, Haidian District, Beijing, 100871, China.
*Corresponding author. Email: wangjing2015@zju.edu.cn (J.W.); jijian@zju.edu.cn (J.J.)
†These authors contributed equally to this work.

molecular diffusion (*48*–*50*). In contrast to the passive diffusion of drugs, our PMI strategy features active repulsion of dynamic mucus-like liquid and temporary opening of tight junctions for robust drug penetration. The compression of the porous structure under pressure is supposed to facilitate the propulsion of the loaded solution toward the surface, and simultaneously, the pores on the surface can expedite liquid extrusion and realize microinjection for rapid penetration across barriers (Fig. 1). We have successfully demonstrated the capability of our PMI platform to achieve efficient and safe penetration for various functional agents under low-pressure levels. Notably, the PMI strategy enabled an unprecedented penetration depth of model protein bovine serum albumin (BSA) across endothelial barriers, reaching 150 μm at a pressure of 100 kPa within only 60 s. The penetration distance of small molecules showed a linear relationship with the square root of pressure, providing precise control over delivery depth according to Darcy's law. Unusually, the delivery depth of macromolecule drugs was unexpectedly enhanced under higher pressure, possibly due to the superelastic behavior of the endothelium. By combining with an interventional balloon, this PMI strategy could further facilitate endoluminal drug delivery into blood vessels, gastrointestinal tracts, and tracheas. On the basis of this porous-coated balloon (PCB), we conducted ultrafast delivery of 4-octyl itaconate (OI) into rat carotid artery in vivo, which achieved the inhibition of acute inflammation and promoted endothelium regeneration after balloon angioplasty (*51*, *52*). Collectively, this PMI strategy presents a reliable paradigm for achieving straightforward endoluminal drug delivery across biological barriers, thereby facilitating the advancement of precision therapy and combination medical devices.

RESULTS

Construction of PLEL elastic spongy coating

To fabricate this hydrophilic and elastic porous platform, we developed triblock copolymers polylactic acid–polyethylene glycol–polylactic acid [PLA-PEG-PLA (PLEL)] with soft and hydrophilic PEG segments, hard PLA segments, and cross-linkable double bond caps (Fig. 2A) (*43*, *45*). The synthesis of PLEL copolymer is illustrated in fig. S1A. The ^{1}H nuclear magnetic resonance (NMR) spectroscopy (fig. S1B), gel permeation chromatography (GPC) (fig. S1C), and the Fourier transform infrared (FTIR) spectrum (fig. S1D) verified the successful synthesis of copolymers with different mass ratios of PEG and PLA (table S1). We performed a set of mechanical tests to optimize the ratio of soft and hard segments. On the basis of the tensile testing (Fig. 2, B and C), the Young's moduli of PLEL204 (50 wt % PEG), PLEL210 (20 wt % PEG), and PLEL220 (10% PEG) were measured as 4.01 ± 0.41 MPa, 8.60 ± 1.15 MPa, and 299 ± 25 MPa, respectively. The high content of PEG in PLEL204 resulted in weak and brittle mechanical performance, potentially leading to undesirable rupture during compression. Moreover, the thermograms (fig. S2) indicated that the glass transition temperature (T_g) increased from −27.3° to 19.2°C and 35.1°C for PLEL204, 210, and 220, respectively. Correspondingly, the PLEL210 exhibited moderate mechanical strength at room temperature and showed rapid softening at physiological temperature (Fig. 2C). In contrast, the modulus of PLEL220 remained 58-fold greater than that of PLEL210. Since the thermo-softening property should be beneficial for maintaining its porous morphology during the drug loading and realizing facile deformation under gentle pressure, we thus chose PLEL210 to prepare the elastic porous coating.

Next, the PLEL210 porous coating was fabricated by the ultrasonic spray coating and etching process (Fig. 2E). We first investigated the effect of varying ratios of PLEL and polyvinyl pyrrolidone (PVP) on the coating morphology. As shown in Fig. 2F, all four samples with ratios ranging from 5:5 to 2:8 successfully yielded a porous structure with a white opaque appearance. At ratios of 3:7 and 2:8, spontaneous collapse occurred within these pore structures leading to reduced thickness and total pore volume. Surface analysis revealed that average pore sizes were merely 4.5 and 5.0 μm for ratios of 5:5 and 4:6, respectively (Fig. 2G). The pore size rapidly increased to 7.7 and 10.7 μm when using higher PVP contents (70 and 80%). The pore area on the surface showed same tendency (Fig. 2H).

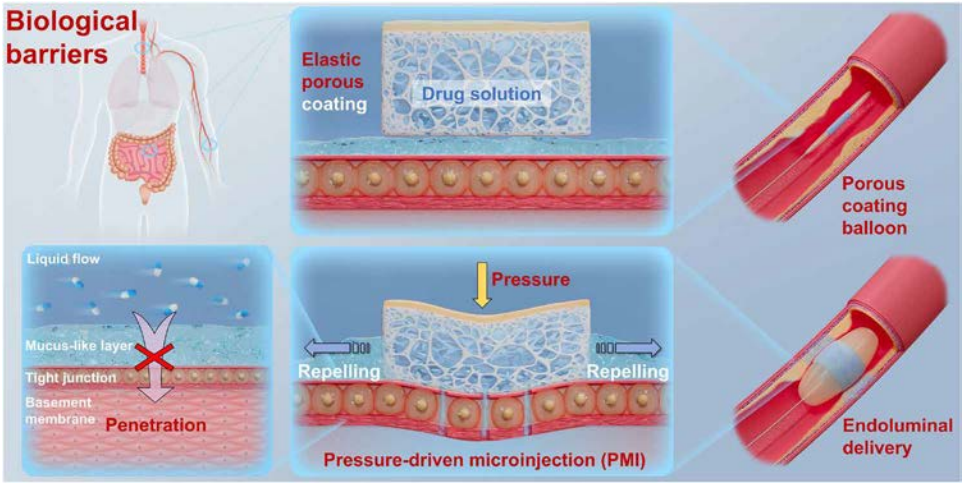

Fig. 1. Schematic illustration of the PMI strategy. The luminal biological barriers, comprising a mucus-like layer, tight junctions, and basement membrane, pose severe obstacles to drug delivery into the tissue. This PMI concept includes capillary adsorption of drug solution, repulsion of dynamic mucus, and localized microinjection, thereby achieving the penetrative drug delivery across barriers. By combining this strategy with medical balloon devices, the endoluminal delivery of functional agents can be accomplished during balloon dilation.

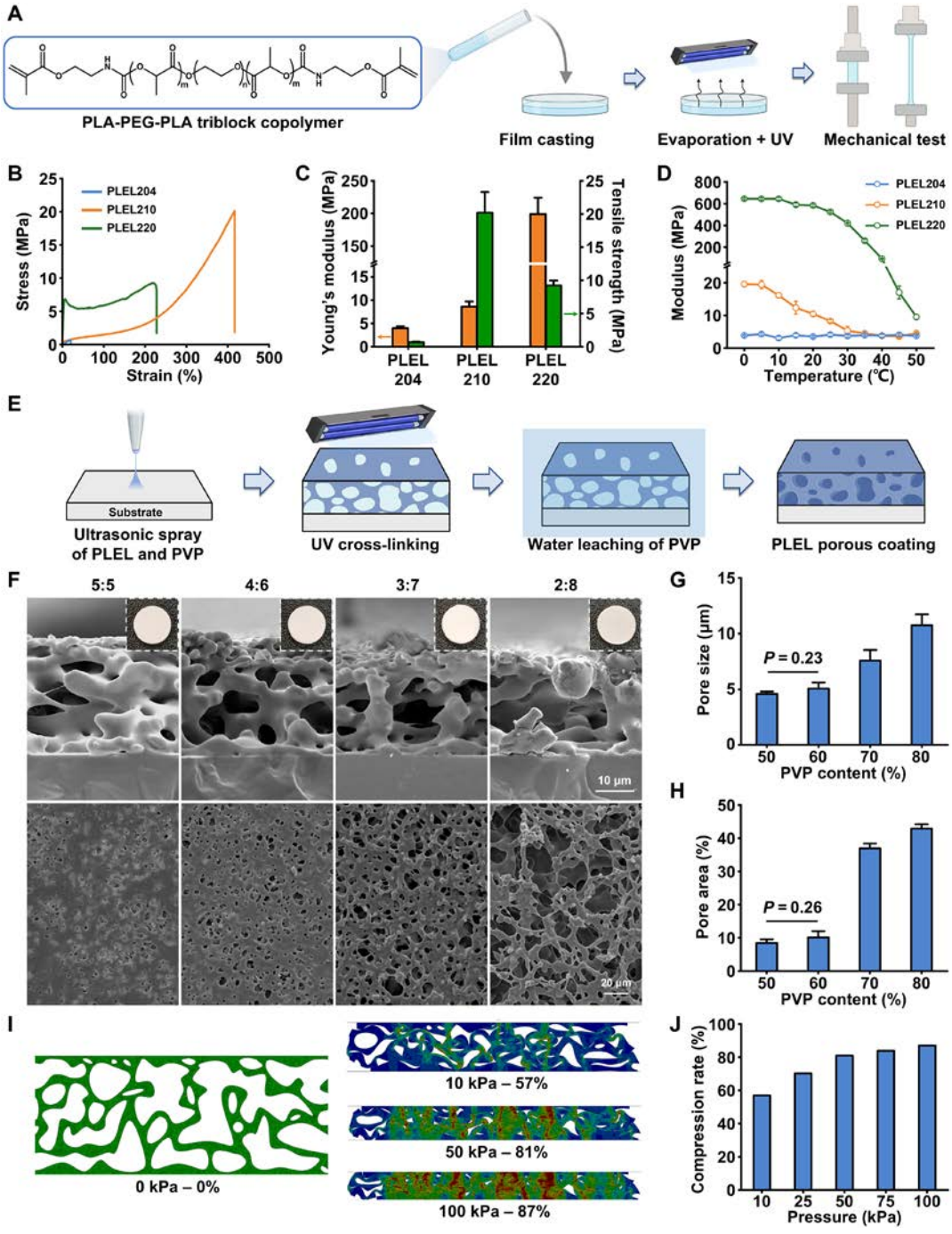

Fig. 2. The preparation of PLEL elastic porous coating. (**A**) Schematic illustration of the elastic PLEL film fabrication. (**B**) The tensile curve of PLEL films. (**C**) The Young's modulus and tensile strength of PLEL films. (**D**) The modulus of PLELs under different temperatures. (**E**) Schematic illustration of the preparation of PLEL spongy coating. (**F**) The scanning electron microscope (SEM) images of cross-sectional and surface structure of spongy coating fabricated by different PLEL:PVP ratios. The inserted pictures are the optical photos of the coatings. (**G**) The pore size and (**H**) pore area on the surface of spongy coating at different ratios. (**I**) Finite element simulation of the compression of porous coating under different pressures. (**J**) The compression rate of porous coating under different pressure. Data are shown as means ± SD from three independent experiments [(C) and (D)] or six independent experiments [(G) and (H)].

Considering that the less pore area on the surface can minimize leakage during delivery, yet high porosity allows for greater drug load capacity, we selected the ratio of 4:6 for further evaluation. The elasticity of our porous coating was verified through the application of finite element analysis (FEA). The Young's modulus of this porous coating was 6.5 MPa by nanoindentation (fig. S3). As shown in Fig. 2 (I and J), under a pressure as low as 10 kPa, the porous area exhibited compression exceeding 50%. Further increase in pressure to 100 kPa resulted in an enhanced compression rate of up to 87%, indicating the capability of liquid extrusion under mild conditions. The elasticity and durability of the porous coating were further demonstrated by pressing at high pressures (fig. S4) and 500-cycle bending test (fig. S5).

The loading and pressure-driven delivery behavior of PLEL porous coating

We chose gelatin hydrogel as a model to investigate the drug delivery capability of our spongy coating under pressure (Fig. 3A). The wicking action of this spongy coating was evaluated using methylene blue (MB) and fluorescein sodium (FLS) as model molecules. As shown in Fig. 3B, the MB solution rapidly ascended to the top of the coating within 2.5 s, indicating the robust wicking effect of interconnected pores. In addition, the green fluorescence signal of FLS was uniformly distributed within the entire spongy coating (Fig. 3C), suggesting a uniform loading of functional agents. The loading efficiency was then evaluated with four different types of molecules, including positively charged small-molecule rhodamine B (RhB), negatively charged small-molecule FLS, macromolecule dextran with a molecular weight of 40,000 (Dex-40k), and negatively charged macromolecule BSA (66 kDa). As shown in Fig. 3D, similar loading efficiency was observed for all tested molecules within the porous coating, indicating convenient and efficient absorption-based loading of functional agents. The restricted diffusion of molecules in complex porous structures enables the PMI strategy to retain drug solution through the intervention process (fig. S6).

To quantify the delivery efficiency of this PMI strategy, we adopted the gelatin gel to simulate the dynamic fluid-wrapped tissues. The drug-penetrated gelatin was redissolved at 37°C, followed by dilution and spectrum analysis. As shown in Fig. 3E, the transfer of RhB dosage amounted to 52.7 ± 5.0% of total loading under the pressure of only 10 kPa. Increasing the pressure resulted in an enhanced delivery dosage, reaching 72.9 ± 8.9% of total loading under the pressure of 100 kPa. Notably, the delivery profile showed a similar tendency when using negatively charged FLS molecules instead. Subsequently, Dex-40k and BSA were studied as macromolecules with varying molecular weights. As shown in Fig. 3F, these macromolecules exhibited similar penetration dosages as small molecules, achieving ~45% penetration under a pressure of 10 kPa and further increasing to around 75% under 100 kPa. The pressure-dependent enhancement of delivery content indicates the efficient delivery of

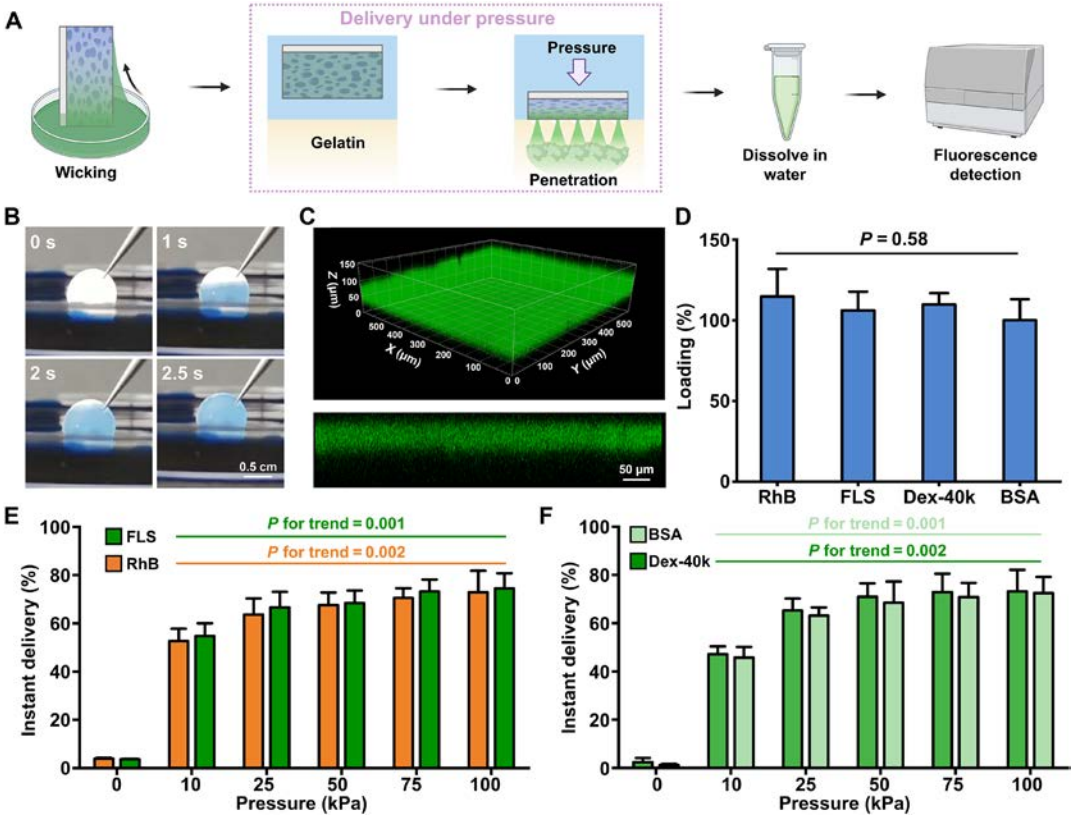

Fig. 3. The controllable loading and pressure-driven delivery of various functional agents. (**A**) The schematic illustration of the wicking effect and the evaluation of instant delivery. (**B**) The optical images of the capillary absorption of MB solution into porous coating. (**C**) The confocal microscopy image of porous coating loaded with FLS. (**D**) The loading of various functional agents into porous coating by a wicking effect. The delivery ability under different pressures of (**E**) small molecules and (**F**) macromolecules. Data are shown as means ± SD from three independent experiments.

functional agents by PMI treatment. Considering the consistency of these results and the FEA simulation, this PMI approach facilitates controllable loading and instant delivery of diverse functional agents.

In vitro evaluation of trans-barrier delivery by PMI treatment

To further evaluate the penetration behavior in real tissue based on our PMI strategy, we used a porcine aorta as a representative model with typical biological barriers (Fig. 4A). The drug-loaded porous coating was pressed on blood vessel to facilitate the repulsion of floating liquid and enable the straightforward penetration of functional agents. The penetration distance was detected using a confocal laser scanning microscope. By adopting a patterned porous coating, RhB delivery was only observed at the site of porous coating, while the flat area showed no penetration (Fig. 4B), highlighting the in situ delivery capability of this PMI strategy. The delivery of small molecules RhB and FLS was then evaluated. As shown in fig. S7, the RhB could deliver to 75 μm at only 10 kPa, then gradually increased to 225 μm at 25 kPa, and lastly reached 252 μm at 100 kPa. The delivery of FLS showed the same tendency as RhB. However, it exhibited shallower penetration depths compared to RhB, reaching only 175 μm at 100 kPa (Fig. 4C). This difference in penetration distance between molecules with different charges may be attributed to negatively charged surface properties of blood vessels (*5*).

Moreover, the size of the functional agents exhibited a marked impact on the depth of penetration. As shown in Fig. 4D and fig. S8, Dex-40k was delivered to about 54 μm at 10 kPa. The delivery depth gradually increased to 66, 72, and 75 μm, respectively, as the pressure rose to 25, 50, and 75 kPa. However, an enhancement in penetration distance was observed when the pressure reached 100 kPa with a depth of 175 μm. When using BSA as a model protein (66 kDa, 7.2 nm), the penetration depth at 50 kPa decreased to 60 μm (Fig. 4E). Similarly, the delivery depth of BSA also exhibited a substantial increase from 66 μm at 75 kPa to 150 μm at 100 kPa. Notably, this unprecedented penetration of functional species was accomplished through a gentle pressing procedure lasting only 60 s, underscoring an unparalleled capability for the deep administration of diverse therapeutic agents in practical applications.

Since the tunica media of blood vessels primarily comprises smooth muscle cells (SMCs) and a loosely arranged extracellular matrix, we postulate that this loose combination can function as a porous medium, facilitating fluid infiltration through ample interstitial space. In this context, we proposed a mathematical model to elucidate the correlation between penetration depth and pressure. Darcy's law describes the fluid flow in porous materials, stating that the flow rate Q of the fluid is linearly related to the pressure difference ΔP (*53*–*55*). The flow rate Q equals cross-sectional area A multiplied by velocity (Eq. 1), where ε is the porosity, μ is the fluid viscosity, and k is the structural coefficient of porous media. By solving Eq. 1, it was deduced that penetration distance x is proportional to the square root of ΔP (Eq. 2).

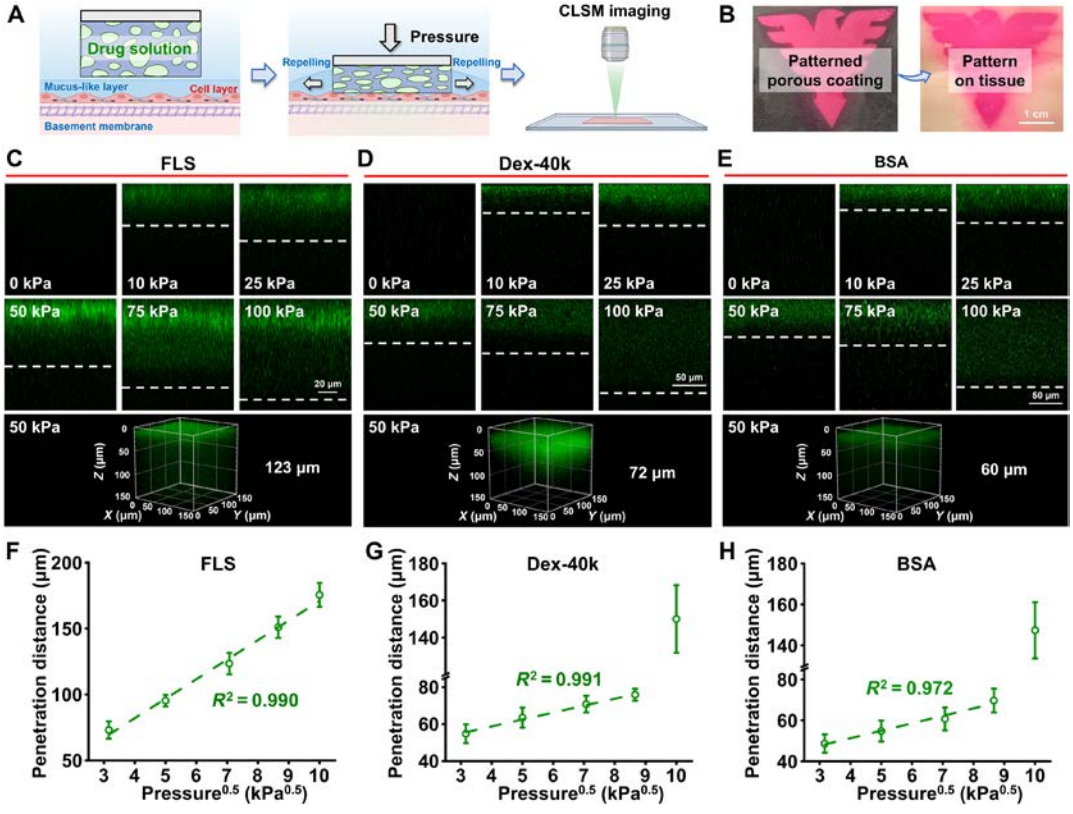

Fig. 4. The penetration distance of functional agents under pressure on porcine aorta model. (**A**) The schematic illustration of the delivery of drug solution crossing obstacles under pressure. (**B**) Images of patterned delivery of functional agents. The confocal microscopy images of the penetration of (**C**) FLS, (**D**) Dex-40k, and (**E**) BSA under different pressures. The relationship between penetration distance and pressure$^{0.5}$ of (**F**) FLS, (**G**) Dex-40k, and (**H**) BSA. Data are shown as means ± SD from three independent experiments. R^2, coefficient of determination. CLSM, confocal laser scanning microscope.

$$Q \equiv A\varepsilon \frac{dx}{dt} = A\frac{k}{\mu}\frac{\Delta P}{x} \quad (1)$$

$$x = \left(\frac{2k\Delta P}{\mu\varepsilon}\right)^{0.5} t^{0.5} \quad (2)$$

As shown in Fig. 4F, a linear relationship was observed between the penetration distance (x) of small-molecule FLS and the root number of pressures ($P^{0.5}$). Similarly, for macromolecules Dex-40k and BSA, a linear relationship was also presented at the pressure between 10 and 75 kPa (Fig. 4, G and H), indicating the controllable delivery of functional agents across biological barriers by our PMI strategy. Unexpectedly, a marked surge appeared as the pressure increased from 75 to 100 kPa for macromolecules. In contrast to the relatively limited diffusion profile observed at low pressure, the penetration depth of macromolecules at 100 kPa exhibited a similarity to that of small molecules, implying comparable permeability for both small and macromolecules under high pressure.

Previous researches have demonstrated that biological tissues, such as epithelial sheets, exhibit a characteristic superelastic behavior enabling them to undergo and withstand three-dimensional deformations under luminal pressure (*56*, *57*). The pressure-induced tension can generate a tensional plateau over several-fold areal strains. Inspired by this superelastic behavior, we assume that our PMI process might cause a similar tensional plateau to the underlying biological barriers and achieve a temporary enhancement of the permeability for macromolecules at a critical pressure (Fig. 5A). We used an incompressible Neo-Hookean model for biological barriers and apply standard shooting method to solve this set of differential equations (the Supplementary Materials). Consider a thin cell layer of shear modulus G, thickness t, surface tension γ, and radius R subject to the applied pressure p. The system is controlled by two dimensionless parameters: $P = pR/Gt$ (characterizing the strength of the applied pressure) and $\Gamma = \gamma/Gt$ (characterizing the strength of the surface tension). By substituting the physiological parameters of porcine artery, including $G = 50$ to 100 kPa (*58*), $t = 1$ to 2 μm (*5*, *7*), and $\gamma = 72$ mN/m, we calculated the surface tension constant

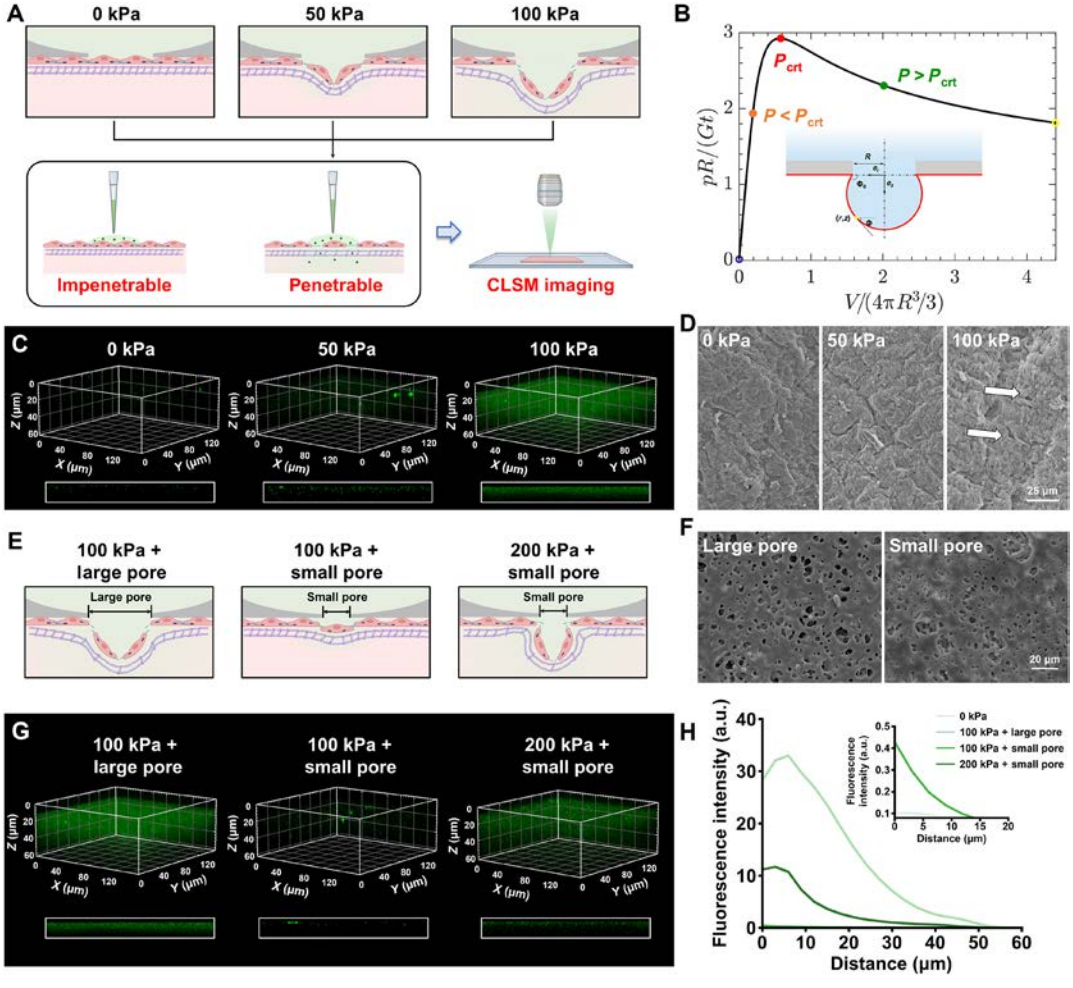

Fig. 5. The mechanism of molecule penetration under pressure. (**A**) The schematic illustration of the PMI process at different pressures and evaluation of the integrity of biological barriers. (**B**) The calculated model of PMI strategy ($\Gamma = 0.5$). (**C**) The confocal images of BSA diffusion into vessel wall after PMI treatment under different pressures. (**D**) The SEM images of vessel wall after PMI treatment under different pressures. (**E**) The schematic illustration of the PMI process with different pore sizes. (**F**) The SEM images of porous coatings with different surface pore sizes. (**G**) The confocal images and (**H**) fluorescence distribution of BSA diffusion into vessel wall after pressing by different pore sizes. a.u., arbitrary units. CLSM, confocal laser scanning microscope.

$\Gamma = 0.36$ to 1.44. Figure 5B shows the pressure-volume curve for $\Gamma = 0.5$. The critical instability pressure P_{crt} appeared at $P = 2.85$, which correlated to the applied pressure $p_{crt} = 82$ kPa ($R = 5$ μm).

According to this superelastic model, the endothelial barrier is expected to exhibit a strain-softening behavior when the applied pressure exceeds 82 kPa, leading to substantial stretch and temporary opening of the extracellular matrix similar to neutrophil-induced opening of basement membrane (*59*). To test this hypothesis, we dipped BSA–fluorescein isothiocyanate (FITC) solution into the blood vessel immediately after applying the PMI process. As shown in Fig. 5C, the green fluorescence signal showed similar distribution between the vessels before and after 50 kPa PMI treatment. However, when the pressure increased to 100 kPa, we observed the diffusion of BSA-FITC into the vessel, confirming the temporary opening of the endothelium barrier (fig. S9). In addition, we examined the blood vessel structure following the application of different pressures. As shown in Fig. 5D, the endothelium remained intact at 50 kPa and showed rough morphology and wrinkles at 100 kPa, indicating a higher tension at extruding site and the temporary opening of endothelium barrier. However, the holes are relatively minimal compared to invasive strategies (such as microneedles and drug crystals), thus beneficial for the recovery and regeneration of endothelium.

Moreover, this superelastic model suggested an inverse relationship between the critical instability pressure (p_{crt}) and pore size R (Fig. 5E). The permeability of blood vessels showed minor changes before and after pressing by a nonporous sheet at 100 kPa, highlighting the necessity of porous structure in this PMI strategy (fig. S10). We next fabricated a porous coating with smaller pore sizes of 2.8 μm, compared to our original porous coating with a pore size of 5.0 μm (Fig. 5F and fig. S11). According to our model, reducing the pore size from 5.0 to 2.8 μm increased p_{crt} from ~82 to ~150 kPa. As shown in Fig. 5G, the fluorescence distribution in vessel wall showed similar behavior before and after PMI treatment at 100 kPa by porous coating with small pore size, while the green signal distributed markedly in blood vessels at the same pressure by coating with large pore size, indicating that larger pore size could facilitate the penetration of functional agents. The BSA diffusion into vessel wall was only observed when the pressure increased to 200 kPa for small pore size (Fig. 5H). Therefore, the deep delivery of functional agents by this PMI strategy was achieved through the stretching and temporary opening of biological barriers and controlled by applied pressure and pore size.

To further extend the applicability of this superelastic model to other tissues, we calculated pressure-volume curves with varying surface tension constant Γ. As shown in fig. S12A, P_{crt} exhibits a decreasing trend in response to the reduction of Γ. Further graphical analysis revealed a linear relationship between P_{crt} and Γ (fig. S12B)

$$P_{crt} = 1.98\Gamma + 1.88 \tag{3}$$

and Eq. 3 can be rewritten as

$$p_{crt}R = 1.88Gt + 1.98\gamma \tag{4}$$

indicating a linear relationship between $p_{crt}R$ and Gt (fig. S12C). To validate this model, we used the intestine as a test case. The biological barriers of intestine are primarily composed of a monolayer of epithelial cells with a shear modulus $G = 10$ kPa and thickness $t = 20$ μm (*60*). By substituting these parameters into the model, the epithelial barrier is expected to open when the pressure exceeds 103 kPa with the large pore size of 5 μm or when the pressure exceeds 184 kPa with the small pore size of 2.8 μm. This conclusion was verified by investigating the permeability of intestine barriers. As shown in fig. S12D, the barrier remained intact after PMI treatment at 50 kPa for large pores, while the green signal markedly spread into intestines at 150 kPa. For small pores, the permeability of intestine barriers changed only when the pressure increased to 200 kPa. Therefore, we believe that this superelastic model is applicable to diverse biological barriers, thereby enhancing the design of porous coatings for improving drug penetration.

Ex vivo evaluation of delivery crossing various barriers on balloon

To verify the potential of our strategy for in vivo applications, we combined the elastic porous coating with balloon to realize endoluminal administration (Fig. 6A) (*61*). As shown in Fig. 6B, the porous coating was solid and stable on balloon. The green fluorescence signal of FLS was uniformly distributed within the spongy coating, suggesting a homogeneous loading of functional agents. Furthermore, both cross-sectional and surface analysis confirmed that the porous structure resembled the flattened porous coating (fig. S13), thus confirming the successful construction of PLEL spongy coating on balloons.

We then used the PCBs to verify the penetration of functional agents over biological barriers under pressure. Dex-40k served as the model macromolecular drug. A relatively thin carotid artery (with a diameter of 1.2 mm) was applied to simulate the stenotic artery during treatment. On the basis of the degree of vascular strain, the exerted pressures on vessel wall reached ~37.5 and 97.5 kPa at 1 and 3 atm inflation, respectively (*62*). As shown in Fig. 6C, at a pressure of 1 bar, the green signal permeated half of the vessel wall, reaching a penetration depth of 59 ± 10 μm (Fig. 6D). This depth correlated well with the theoretically calculated value of 66 μm. In addition, the distribution of Dex-40k decreases progressively with increasing penetration depth, characteristic of diffusion-limited transport behavior (*63*). Unexpectedly, a relatively homogeneous distribution of Dex-40k in blood vessels was observed under 3 atm pressure (97.5 kPa), consistent with convection-dominated delivery behavior (*64*), further confirming the superelastic behavior-induced opening of endothelial barriers. However, because of the limitation of the vascular wall thickness, the ex vivo experiment was only able to confirm convective transport behavior under 3 atm and could not measure the maximum penetration depth. The total fluorescence intensity also showed a marked increase with the elevated pressure (Fig. 6E). Considering the inevitable endothelial injury in clinical intervention therapies, we further evaluated the delivery of Dex-40k to denuded vessels. As shown in fig. S14, a homogeneous drug distribution across the entire vascular was observed under both 1 atm (37.5 kPa) and 3 atm (97.5 kPa) balloon dilation, further demonstrating the penetration capabilities of our PMI strategy in the treatment of CVDs. These results of delivery behavior in luminal tissues were consistent with the findings from the planar experiments in vitro, indicating the efficient drug delivery capabilities of PCBs.

Furthermore, trachea and intestine were examined as the model of mucin barrier and epithelial barrier. Notably, both tracheal and intestinal walls exhibited substantial distribution of green signal (Fig. 6F), further confirming robust penetration across biological barriers under applied pressure. Therefore, our PMI strategy could achieve the in vivo endoluminal administration under relatively low pressure across various obstacles.

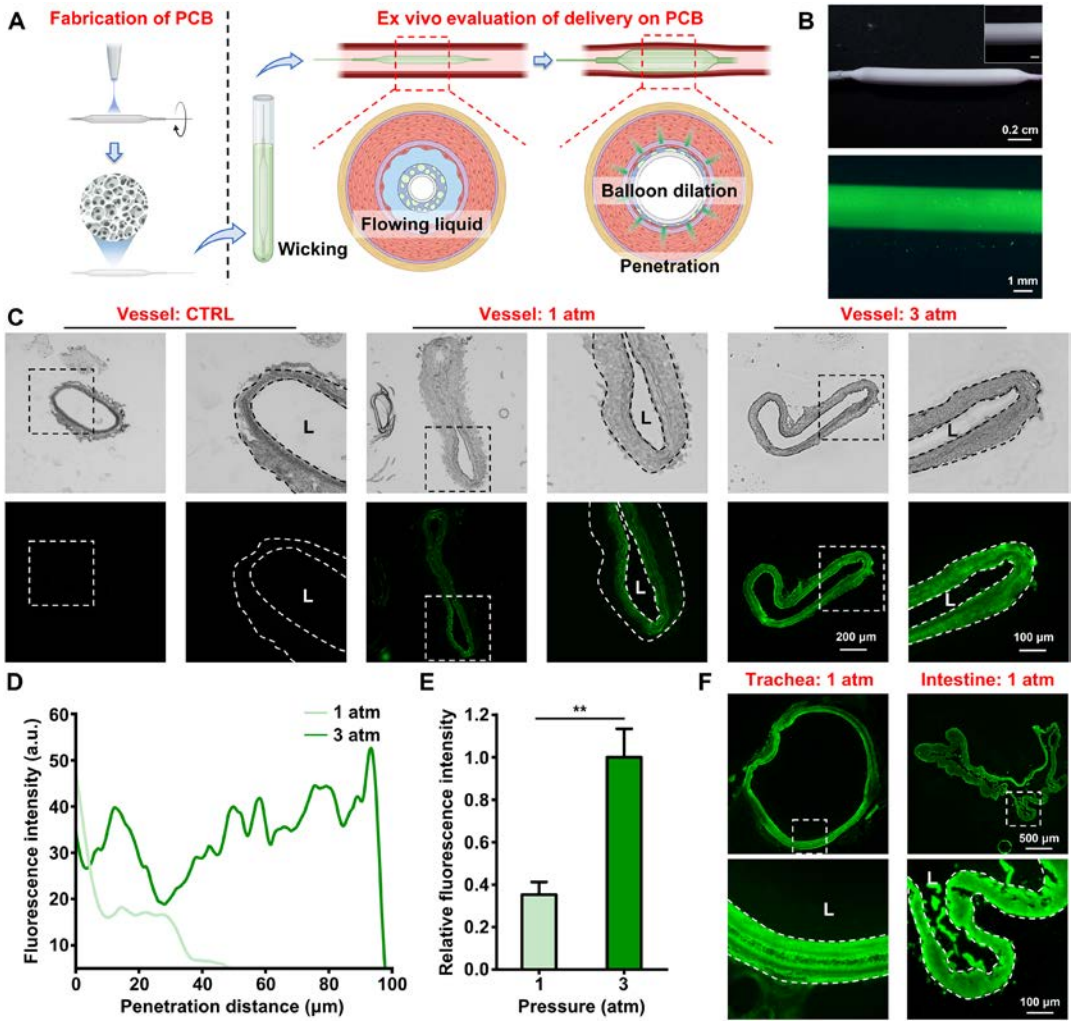

Fig. 6. The ex vivo evaluation of endoluminal administration based on PCBs. (**A**) Schematic illustration of the fabrication of PCBs and ex vivo evaluation of drug delivery. (**B**) The optical and fluorescence photos of PCBs after dilation. The inserted photos are the magnified photos of the surface of balloons. Scale bar, 0.2 cm. (**C**) The cryosection of rat blood vessels before dilation and dilation under 1 and 3 atm. (**D**) The analysis of Dex-40k distribution in blood vessels under 1 and 3 atm. (**E**) The fluorescence intensity of Dex-40k in vessels under 1 and 3 atm. (**F**) The cryosection of rat trachea and intestine after balloon dilation under 1 atm. Data are shown as means ± SD from three independent experiments. $^{**}P < 0.01$. L, lumen.

In vivo evaluation of OI-loaded PCBs

To evaluate the therapeutic capability of PCBs, we performed in vivo animal experiments using a rat common carotid artery injury model (Fig. 7A). We first evaluated the instant delivery of functional agents crossing endothelial barriers by PCBs. As shown in Fig. 7B, macromolecule Dex-40k could penetrate through the obstacles and distribute in the whole blood vessel under 3 atm (97.5 kPa), indicating the breakthrough of the endothelium under pressure. Then, OI, an anti-inflammatory drug, was delivered to realize the inhibition of neointima hyperplasia (*42*, *65*). Liquid chromatography–mass spectrometry (LC-MS) analysis was applied to investigate the delivery amount of OI across barriers. As shown in Fig. 7C and fig. S15, 83.8 ± 3.4% OI was successfully delivered into blood vessel, confirming efficient drug penetration. To confirm the translational potential of the PCBs, the in vivo evaluation of drug delivery into denuded vessel was performed. As shown in fig. S16, both small-molecule RhB and macromolecule Dex-40k demonstrated uniform distribution within the media layer of the vessel wall and followed a convective transport pattern, consistent with the results from ex vivo experiments.

Since acute inflammation in the early stage plays a central role in SMC proliferation, we examined the inflammatory responses after 3 days of intervention. As shown in Fig. 7D, the expression of *CD68* declined in the PCB group compared with the injury group, indicating the inhibition of inflammatory cell infiltration. The expression of interleukin-6 (*IL-6*), *IL-1*β, and tumor necrosis factor–α (*TNF*-α) was all down-regulated, suggesting a lower acute inflammatory effect. In addition, the significant promotion of OI-target genes heme oxygenase-1 (*HO-1*) and NAD(P)H dehydrogenase quinone 1 (*NQO-1*) indicated the effective delivery of OI through the porous balloon. The up-regulation of calponin 1 (*CNN1*) and α–smooth muscle actin (α-*SMA*) showed the suppression of SMC proliferation and phenotype switch. The Western blot analysis showed the same trend. While the expression of cluster of differentiation 68

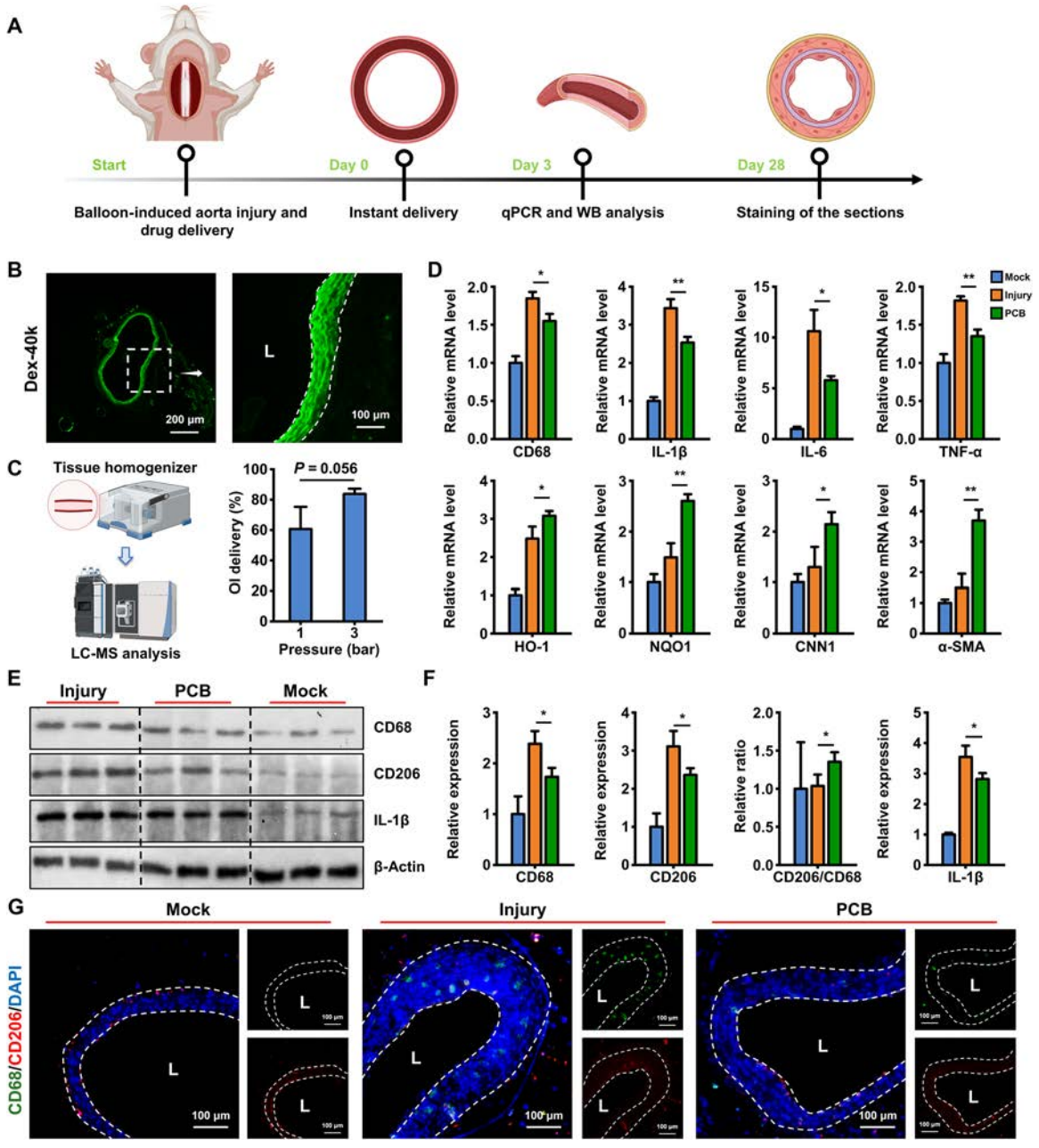

Fig. 7. The in vivo evaluation of PMI strategy and the analysis of acute inflammation. (**A**) The schematic illustration of the in vivo evaluation of PCBs in rat carotid injury model. (**B**) The instant delivery of Dex-40k into rat common carotid artery. (**C**) The content of OI delivered into blood vessel under different pressures in vivo. ($n = 3$). (**D**) The quantitative polymerase chain reaction (qPCR) and (**E**) Western blot (WB) analysis of inflammatory effect after 3 days. (**F**) The statistical results of Western blot analysis. (**G**) The immunofluorescence staining of CD68 (green) and CD206 (red) of the mock group, the injury group, and the PCB group after 1 week. Data are shown as means ± SD from three independent experiments. $^{*}P < 0.05$ and $^{**}P < 0.01$. L, lumen.

(CD68) and mannose receptor (CD206) both decreased in the PCB group, the ratio of CD206/CD68 slightly increased, showing the anti-inflammatory effect of OI delivery, which was consistent with the decrease of IL-1β (Fig. 7, E and F). After the intervention for 1 week, the immunofluorescence staining of CD68 and CD206 was performed. As shown in Fig. 7G, a large quantity of green signal (CD68) appeared in the medium of blood vessels of the injury group, indicating the accumulation of macrophages. In addition, only 19.3% of the green signals overlapped with the red signals (CD206), suggesting a strong acute inflammation. By contrast, the CD68 expression was massively down-regulated in the PCB group, 78.3% of which overlapped with the expression of CD206, indicating the inflammatory regulation effect of PCBs. Therefore, our PCB method inhibited the acute inflammatory effect due to the penetrative delivery of OI by the PMI strategy. The suppression of acute inflammation holds the potential to mitigate the neointima hyperplasia from the upstream (*42*).

The neointima after intervention for 4 weeks was next evaluated. As shown in Fig. 8A, the intima in the injury group thickened

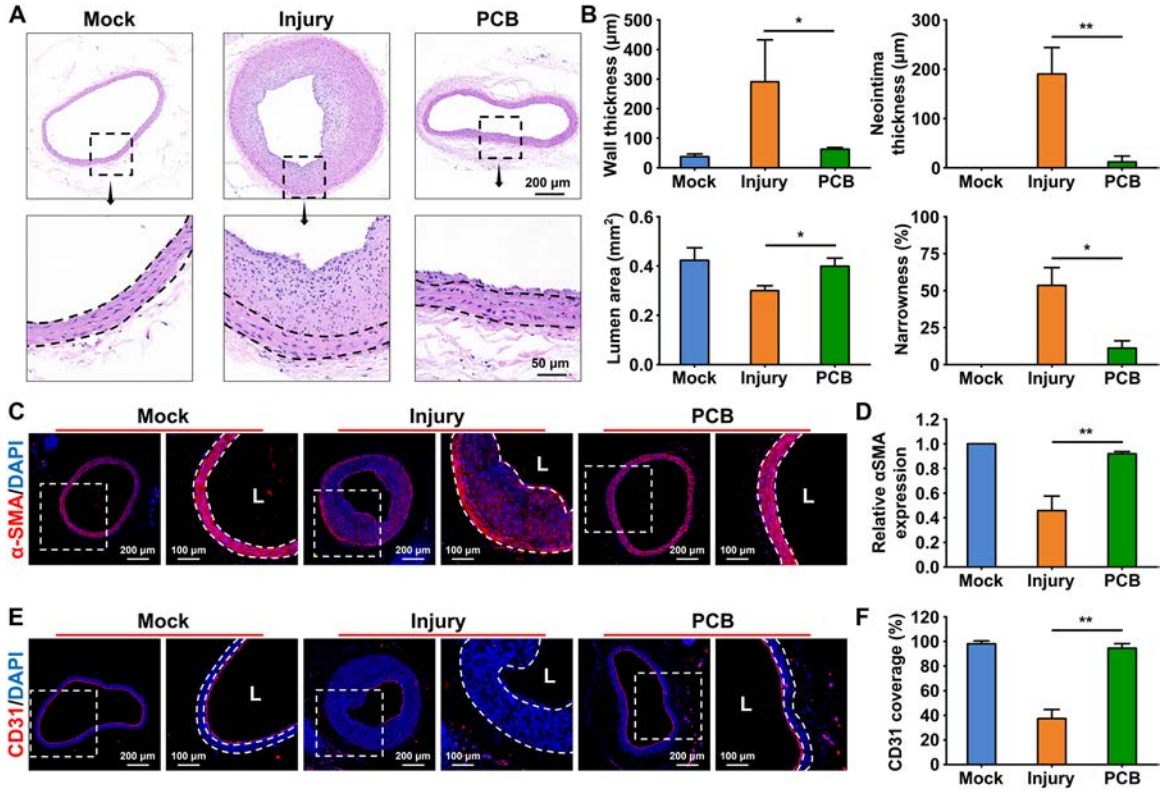

Fig. 8. The characterization of neointima hyperplasia after 4 weeks. (**A**) The hematoxylin and eosin staining of blood vessels. (**B**) Wall thickness, neointima thickness, lumen area, and narrowness of injury and PCB groups. (**C**) The immunofluorescence staining of α-SMA (red) and (**D**) the relative expression of α-SMA in normal blood vessels, the injury group, and the PCB group. (**E**) The immunofluorescence staining of CD31 (red) and (**F**) the ratio of CD31 coverage of normal blood vessels, the injury group, and the PCB group. Data are shown as means ± SD from three independent experiments. *$P < 0.05$ and **$P < 0.01$. DAPI, 4′,6-diamidino-2-phenylindole. L, lumen.

markedly, while the intima hyperplasia was significantly inhibited in the PCB group, as the average thickness of vessel wall and neointimal decreased from 299 ± 141 μm to 63.0 ± 5.0 μm and 199 ± 68 μm to 17.5 ± 9.3 μm, respectively (Fig. 8B). In addition, the ratio of neointimal stenosis declined from 55.3 ± 15.7% to 11.1 ± 6.3%, indicating the successful suppression of neointima hyperplasia. Then, the immunofluorescence staining of α-SMA and platelet endothelial cell adhesion molecule-1 (CD31) was performed to verify the regulation of SMC proliferation and repair of endothelium. As shown in Fig. 8C, the α-SMA expression (red) was suppressed in the injury group, indicating the phenotype switch to synthetic and resulting in the overproliferation of neointima. The thorough penetration of OI inhibited the phenotype switch of SMCs in the PCB group, leading to the much higher expression of α-SMA (Fig. 8D) and a thinner neointima than that in the injury group. Unexpectedly, the ratio of CD31 coverage in the PCB group for 1 week reached more than 80%, while the injury group was barely covered by endothelial cells (fig. S17). After 4 weeks, we still observed a discontinuous expression of CD31 (red) in the injury group (Fig. 8, E and F). By contrast, the CD31 coverage in the PCB group showed no difference with normal vessels, suggesting the regeneration of an intact endothelium. In addition, the injury group still showed strong inflammation after 4 weeks, while the CD68 expression of the PCB group almost disappeared (fig. S18). Therefore, this PMI strategy realized the OI delivery into the medium with minimal damage to endothelium, achieving the rapid regeneration of endothelium and suppression of SMC proliferation, which provided a promising way to inhibit neointima hyperplasia.

DISCUSSION

In summary, we designed a PMI strategy to tackle the obstacles of biological barriers to drug delivery. Our strategy realized controllable loading and ultrafast penetration of various functional agents crossing biological barriers by the compression of elastic porous coating. Notably, the macromolecule BSA achieved a penetration distance into blood vessels (more than 150 μm) after pressing for only 60 s. The delivery distance of functional agents was controllable according to Darcy's law, which was linearly related to the root number of applied pressures. On the basis of the superelasticity and strain-softening behavior of cell layers, we demonstrated that the marked enhancement in the delivery distance of macromolecules under high pressure was attributed to the stretching and temporary opening of biological barriers, facilitating the efficient convection-based drug delivery with minimal damage to endothelium. In addition, by combining elastic porous coating with balloons, we achieved the endoluminal delivery of hydrophilic biomacromolecules into vessels, intestines, and trachea, which was unattainable by conventional drug-coated balloons. Last, as a proof of concept, the PCBs delivered anti-inflammatory drug OI into the media of blood vessels, leading to a marked reduction in macrophage recruitment and neointima hyperplasia postballoon angioplasty.

This study has limitations. This work primarily used healthy vascular models with integrated endothelium. However, in complicated pathological models such as atherosclerosis, the presence of fibrous caps and calcified plaques markedly affects drug delivery efficiency (*66*). Future studies should focus on investigating the delivery behavior and drug distribution in pathological vessels. Besides, the quantitative assessment of delivery distance in ex vivo experiments is limited by the thickness of vessel wall, requiring further investigation using diversified vessel models. Moreover, detailed studies using diseased animal models should be conducted to comprehensively evaluate the therapeutic mechanisms and enhance the translational relevance toward clinical applications.

This work supports further in-depth assessment of endovascular drug delivery dynamics and associated therapeutic outcomes. While current results successfully demonstrated the deep delivery of hydrophilic biomacromolecules across vascular barriers, further research is warranted to ensure sustained therapeutic efficacy in tissue. Given that drug-coated balloons now used in clinical practice predominantly carry hydrophobic agents, it is also essential to further develop and optimize the delivery modalities of PCBs for hydrophobic drugs. This PMI strategy provides a promising technique for overcoming biological barriers and precise delivery of biological therapeutics, benefiting the design and development of interventional medical devices.

MATERIALS AND METHODS

Materials

D,L-lactide, PEG ($M_n = 2000$), 2-isocynatoethyl methacrylate (IEM), gelatin, OI, MB, RhB, and FLS salt were purchased from Macklin (Shanghai, China). Stannous octoate [$Sn(Oct)_2$], 4-methoxyphenol, benzophenone (BP), PVP ($M_w = 40{,}000$), and FITC-labeled dextran (M_n = 40,000) were obtained from Sigma-Aldrich. FITC-labeled BSA was obtained from Feiyu Bio (Nantong, China). Anti-CD31 antibody (SAB5700639), anti–α-SMA antibody (SAB5702823), and anti-CD68 antibody (SAB5702269) were purchased from Sigma-Aldrich. Anti-CD206 antibody (PA5 to 101657) was purchased from Thermo Fisher Scientific. The deionized (DI) water (>18 megohm cm) used in all experiments was purified with a Millipore Milli-Q water purification system.

Synthesis of PLEL copolymers

PEG ($M_n = 2000$) was used to initiate ring opening polymerization of D,L-lactide in the presence of $Sn(Oct)_2$ as a catalyst. Typically, PEG was added into a 50-ml three necked round-bottomed flask followed by a drying step at 100°C for 2 hours under vacuum. Then, D,L-lactide was added under a dry argon atmosphere. The mixture was stirred at 100°C for 10 min under an argon atmosphere and then heated up to 140°C. Next, $Sn(Oct)_2$ was added under a dry argon atmosphere. After reaction for 6 hours, 4-methoxyphenol was added to the reaction as inhibitor. Excess IEM was dissolved in dried toluene and added into the reactor dropwise under a dry argon atmosphere. The acrylation reaction was performed for 20 min. The reactant was cooled to room temperature and dissolved in dichloromethane, followed by precipitation in excess ethanol. The product was dried under vacuum at room temperature for 48 hours. The molecular structure and composition of the PLEL triblock copolymer were determined by 1H NMR (AVANCE NEO 400, Bruker) and FTIR (Nicolet iS20, Thermo Fisher Scientific) spectroscopy. The molecular weight and distribution were tested by GPC (1515, Waters).

Evaluation of the mechanical properties of the PLEL copolymers

The PLEL copolymers and photoinitiator BP were sprayed on a glass substrate to fabricate polymer films with a thickness of 100 μm and then were cross-linked by ultraviolet (UV) irradiation of 2 min. Five milligrams of polymer was cut from the film for the detection of T_g by the differential scanning calorimetry (DSC; Discovery DSC 25, TA). Then, the film was tailored to 0.5 cm by 2 cm. The samples were used in dynamical mechanical analysis (DMA; Discovery DMA 850, TA) to evaluate the modulus of the PLEL copolymers at different temperatures. The extruded curves of the polymers were detected by a universal testing machine (UTM2102, Shenzhen Suns Technology Stock, Shenzhen, China).

Construction of the cross-linked PLEL microporous coating

The PLEL spongy coating was fabricated by an ultrasonic spray system (Ruidu Photoelectric Technology Co. Ltd., Shanghai). PLEL, PVP, and BP were dissolved in the mixture of CH_2Cl_2 and ethanol with a ratio of 1:1. The mass of BP was 1/200 of the total mass of PLEL and PVP. The initial coating was sprayed on a substrate and then was cross-linked by UV for 5 min. The microporous structure was obtained by the immersion of cross-linked coating into DI water for 30 min. The coating was lastly blown dry by nitrogen. Scanning electron microscopy (EM-30+, COXEM, South Korea) was performed to observe the microstructure formation within the PLEL coating.

Compression ability analysis of porous coating

The Young's modulus of the porous coating in the liquid phase was tested using nanoindentation (Piuma), and the probe modulus was selected as 48.8 N/m. The data structure was simulated using the Hertzian model. The FEA was performed using the ABAQUS simulation software system to simulate the mechanical properties of the porous coating. The density of the polymer was set to 1 g/cm^3, and the Poisson's ratio was set to 0.45. We drew a porous morphology, according to the real morphology of porous coating. The force-bearing surface was set to be rigid, and the loading time of the force was 1 s. To facilitate calculation, a two-dimensional surface mesh was constructed, in which the mesh type was CPS4R linear quadrilateral reduced integration element, and the total number of elements was 200,000.

Loading and release under pressure of functional agents

Ten microliters of solution was dripped on the PLEL spongy coating for a wicking effect, and then the coating was rinsed with phosphate-buffered saline (PBS) three times. The content of functional agents in the rinsing solution was measured using a fluorescence spectrophotometer. The total loading dosage of functional agents was calculated by subtraction of the total solute in the initial solution and washing solution.

The loaded PLEL coating was then immersed in 1 ml of PBS for 2, 5, and 10 min to evaluate the leakage of functional agents through delivery. The leakage of functional agents was also measured using a fluorescence spectrophotometer.

A universal testing machine was used to test the instant delivery of solution under pressure. The spongy coating was pressed to

gelatin gel under different pressures. Then, the gelatin gel was dissolved in PBS at 37°C. The total fluorescence intensity of functional agents was calculated by subtraction of the total fluorescence intensity and the fluorescence intensity of gelatin. The content of instant delivery was converted by the standard curve of the fluorescence intensity and concentration of functional agents.

The penetration of functional agents into vessel wall under pressure

The coating was attached to fresh pig aortas through a universal testing machine under different pressures for 60 s. Then, the coating was removed, and the penetration distance of functional agents into the aortas was evaluated using a CLSM (LSM880, Zeiss, Germany).

Ex vivo evaluation of the delivery of functional agents on balloons

The PLEL spongy coating was fabricated on a balloon by ultrasonic spray coating. The blood vessels, intestines, and tracheas were obtained from rats. The denuded arteries were attained by balloon dilation and repeated friction of intima. Balloons with a diameter of 1.5 mm were applied to blood vessels. The experiments on intestines and tracheas were performed by balloons with a diameter of 2.0 mm. A pressure of 1 to 3 atm was applied to exert pressure on tissue and deliver functional agents. The cryosection of the tissues was performed, and the penetration distance was observed using a fluorescence microscope (DS-Ri2, Nikon, Japan).

Following OI delivery, the treated vessels were frozen and subsequently crushed. The OI drug was extracted using TRIzol reagent for 24 hours. After centrifugation, the supernatant was collected, and the concentration of OI was quantified using LC-MS. The LC-MS parameters were consistent with those used in previous studies (*42*).

In vivo evaluation by rat common carotid artery injury model

All animal procedures were approved and conducted following the Guidelines for Care and Use of Laboratory Animals of Zhejiang University (no. 22532). The rats were anesthetized by isoflurane inhalation (5%). A cervical midline incision was made, and the right common carotid artery was dissected. A bare balloon catheter was inserted into the common carotid artery via the external carotid artery and inflated with 2 atm pressure. The inflated balloon was then pulled back and pushed forward rotationally three times to injure the vessels. A porous balloon with OI solution was inserted into the injured vessels again, inflated with 3 atm (97.5 kPa) pressure, and kept at this pressure for 1 min to deliver the solution. After the deflation and withdrawal of the balloon, the surgical site was closed with sutures. The control group was directly sutured after injury. Half of the rats were euthanized at 3 days and the other half at 28 days. The artery samples for 3 days were excised and washed quickly with saline and were frozen in liquid nitrogen directly. The frozen samples were used for Western blot analysis and quantitative polymerase chain reaction analysis to evaluate the protein and mRNA expression of *CD68*, *CD206*, *IL-6*, *IL-1β*, *TNF-α*, *HO-1*, *NQO1*, *CNN1*, and *α-SMA*. The sequences of primers are listed in table S2. The health arteries were adopted as control. The rats were anesthetized, and the right common carotid arteries were harvested for analysis with the left common carotid arteries as controls. Six rats were used in this experiment in total, with three rats for balloon-induced vascular injuries (the injured groups) and three rats for treatment with the coated balloons (the treated groups).

The artery samples for 28 days were excised and washed quickly with saline. The samples were immersed in formalin solution. Then, they were embedded in paraffin for cross-sectional slicing. Five slices were prepared for each section, one of which was performed by hematoxylin and eosin for the histological analysis of the neointimal hyperplasia. Four slides were processed for immunofluorescence evaluation of α-SMA, CD31, CD68, and CD206, respectively. Representative micrographs were taken using a fluorescence microscope (DS-Ri2, Nikon, Japan).

Statistical analysis

All data were obtained from at least three independent experiments with at least three parallel samples per condition in each experiment and expressed as mean ± SD. A test for linear trend was conducted with the use of pressure as a variable. Statistical significance was assessed with the analysis of variance (ANOVA) test and the Student's *t* test. A probability value of $P < 0.05$ is considered statistically significant.

Supplementary Materials

This PDF file includes:

Supplementary Text
Figs. S1 to S18
Tables S1 and S2
References

REFERENCES AND NOTES

1. R. Yang, T. Wei, H. Goldberg, W. Wang, K. Cullion, D. S. Kohane, Getting drugs across biological barriers. *Adv. Mater.* **29**, 10.1002/adma.201606596 (2017).
2. A. Pietroiusti, L. Campagnolo, B. Fadeel, Interactions of engineered nanoparticles with organs protected by internal biological barriers. *Small* **9**, 1557–1572 (2013).
3. H. Viola, K. Washington, C. Selva, J. Grunwell, R. Tirouvanziam, S. Takayama, A high-throughput distal lung air-blood barrier model enabled by density-driven underside epithelium seeding. *Adv. Healthc. Mater.* **10**, e2100879 (2021).
4. A. Tsuda, T. C. Donaghey, N. V. Konduru, G. Pyrgiotakis, L. S. Van Winkle, Z. Zhang, P. Edwards, J.-M. Bustamante, J. D. Brain, P. Demokritou, Age-dependent translocation of gold nanoparticles across the air-blood barrier. *ACS Nano* **13**, 10095–10102 (2019).
5. L. Fu, H. N. Kim, J. D. Sterling, S. M. Baker, M. S. Lord, The role of the cell surface glycocalyx in drug delivery to and through the endothelium. *Adv. Drug Deliv. Rev.* **184**, 114195 (2022).
6. D. Chappell, M. Jacob, K. Hofmann-Kiefer, M. Rehm, U. Welsch, P. Conzen, B. F. Becker, Antithrombin reduces shedding of the endothelial glycocalyx following ischaemia/reperfusion. *Cardiovasc. Res.* **83**, 388–396 (2009).
7. L. Claesson-Welsh, E. Dejana, D. M. McDonald, Permeability of the endothelial barrier: Identifying and reconciling controversies. *Trends Mol. Med.* **27**, 314–331 (2021).
8. N. J. Abbott, A. A. K. Patabendige, D. E. M. Dolman, S. R. Yusof, D. J. Begley, Structure and function of the blood-brain barrier. *Neurobiol. Dis.* **37**, 13–25 (2010).
9. Y. He, Y. Liang, R. Han, W.-L. Lu, J. C. W. Mak, Y. Zheng, Rational particle design to overcome pulmonary barriers for obstructive lung diseases therapy. *J. Control. Release* **314**, 48–61 (2019).
10. C. Song, Z. Chai, S. Chen, H. Zhang, X. Zhang, Y. Zhou, Intestinal mucus components and secretion mechanisms: What we do and do not know. *Exp. Mol. Med.* **55**, 681–691 (2023).
11. J. Byrne, H. W. Huang, J. C. McRae, S. Babaee, A. Soltani, S. L. Becker, G. Traverso, Devices for drug delivery in the gastrointestinal tract: A review of systems physically interacting with the mucosa for enhanced delivery. *Adv. Drug Deliv. Rev.* **177**, 113926 (2021).
12. P. Paone, P. D. Cani, Mucus barrier, mucins and gut microbiota: The expected slimy partners? *Gut* **69**, 2232–2243 (2020).
13. H. C. Zierden, A. Josyula, R. L. Shapiro, H. T. Hsueh, J. Hanes, L. M. Ensign, Avoiding a sticky situation: Bypassing the mucus barrier for improved local drug delivery. *Trends Mol. Med.* **27**, 436–450 (2021).
14. H. Meng, W. Leong, K. W. Leong, C. Chen, Y. Zhao, Walking the line: The fate of nanomaterials at biological barriers. *Biomaterials* **174**, 41–53 (2018).
15. M. Schneider, F. Stracke, S. Hansen, U. F. Schaefer, Nanoparticles and their interactions with the dermal barrier. *Dermatoendocrinol.* **1**, 197–206 (2009).

16. L. Möckl, S. Hirn, A. A. Torrano, B. Uhl, C. Bräuchle, F. Krombach, The glycocalyx regulates the uptake of nanoparticles by human endothelial cells in vitro. *Nanomedicine* **12**, 207–217 (2017).
17. K. Netsomboon, A. Bernkop-Schnurch, Mucoadhesive vs. mucopenetrating particulate drug delivery. *Eur. J. Pharm. Biopharm.* **98**, 76–89 (2016).
18. L. M. Ensign, B. C. Tang, Y.-Y. Wang, T. A. Tse, T. Hoen, R. Cone, J. Hanes, Mucus-penetrating nanoparticles for vaginal drug delivery protect against herpes simplex virus. *Sci. Transl. Med.* **4**, 138ra79 (2012).
19. D. Işık, A. A. Joshi, X. Guo, F. Rancan, A. Klossek, A. Vogt, E. Rühl, S. Hedtrich, D. Klinger, Sulfoxide-functionalized nanogels inspired by the skin penetration properties of DMSO. *Biomater. Sci.* **9**, 712–725 (2021).
20. X. Han, Y. Lu, J. Xie, E. Zhang, H. Zhu, H. Du, K. Wang, B. Song, C. Yang, Y. Shi, Z. Cao, Zwitterionic micelles efficiently deliver oral insulin without opening tight junctions. *Nat. Nanotechnol.* **15**, 605–614 (2020).
21. Z. Fu, D. Ni, S. Cai, H. Li, Y. Xiong, R. Yang, C. Chen, Versatile BP/Pd-FPEI-CpG nanocomposite for "three-in-one" multimodal tumor therapy. *Nano Today* **46**, 101590 (2022).
22. S. Li, Z. Peng, J. Dallman, J. Baker, A. M. Othman, P. L. Blackwelder, R. M. Leblanc, Crossing the blood-brain-barrier with transferrin conjugated carbon dots: A zebrafish model study. *Colloids Surf. B Biointerfaces* **145**, 251–256 (2016).
23. D. T. Wiley, P. Webster, A. Gale, M. E. Davis, Transcytosis and brain uptake of transferrin-containing nanoparticles by tuning avidity to transferrin receptor. *Proc. Natl. Acad. Sci. U.S.A.* **110**, 8662–8667 (2013).
24. J. Rohrer, A. Partenhauser, S. Hauptstein, C. M. Gallati, B. Matuszczak, M. Abdulkarim, M. Gumbleton, A. Bernkop-Schnurch, Mucus permeating thiolated self-emulsifying drug delivery systems. *Eur. J. Pharm. Biopharm.* **98**, 90–97 (2016).
25. I. Pereira de Sousa, B. Cattoz, M. D. Wilcox, P. C. Griffiths, R. Dalgliesh, S. Rogers, A. Bernkop-Schnurch, Nanoparticles decorated with proteolytic enzymes, a promising strategy to overcome the mucus barrier. *Eur. J. Pharm. Biopharm.* **97**, 257–264 (2015).
26. W. Fan, H. Han, Z. Lu, Y. Huang, Y. Zhang, Y. Chen, X. Zhang, J. Ji, K. Yao, ε-Poly-L-lysine-modified polydopamine nanoparticles for targeted photothermal therapy of drug-resistant bacterial keratitis. *Bioeng. Transl. Med.* **8**, e10380 (2023).
27. J. Li, F. Jia, Z. Chen, J. Lin, Q. Lv, Y. Huang, Q. Jin, Y. Wang, G. Fu, J. Ji, Targeted delivery of liver X receptor agonist to inhibit neointimal hyperplasia by differentially regulating cell behaviors. *Biomater. Sci.* **10**, 6354–6364 (2022).
28. Y. Gao, J. Wang, M. Chai, X. Li, Y. Deng, Q. Jin, J. Ji, Size and charge adaptive clustered nanoparticles targeting the biofilm microenvironment for chronic lung infection management. *ACS Nano* **14**, 5686–5699 (2020).
29. W. Yu, J. Shen, C. Ji, P. Zhang, H. Chang, Y. Wang, J. Ji, Microneedle system with light trigger for precise and programmable penetration. *Mater. Horiz.* **10**, 3044–3050 (2023).
30. A. Mohizin, J. K. Kim, Current engineering and clinical aspects of needle-free injectors: A review. *J. Mech. Sci. Technol.* **32**, 5737–5747 (2018).
31. A. Mohizin, D. Lee, J. K. Kim, Impact of the mechanical properties of penetrated media on the injection characteristics of needle-free jet injection. *Exp. Therm. Fluid Sci.* **126**, 110396 (2021).
32. A. Dasgupta, M. Liu, T. Ojha, G. Storm, F. Kiessling, T. Lammers, Ultrasound-mediated drug delivery to the brain: Principles, progress and prospects. *Drug Discov. Today Technol.* **20**, 41–48 (2016).
33. Z. Ma, C. Bourquard, Q. Gao, S. Jiang, T. De Iure-Grimmel, R. Huo, X. Li, Z. He, Z. Yang, G. Yang, Y. Wang, E. Lam, Z.-H. Gao, O. Supponen, J. Li, Controlled tough bioadhesion mediated by ultrasound. *Science* **377**, 751–755 (2022).
34. P. Bakshi, D. Vora, K. Hemmady, A. K. Banga, Iontophoretic skin delivery systems: Success and failures. *Int. J. Pharm.* **586**, 119584 (2020).
35. X. Chen, L. Zhu, R. Li, L. Pang, S. Zhu, J. Ma, L. Du, Y. Jin, Electroporation-enhanced transdermal drug delivery: Effects of logP, pKa, solubility and penetration time. *Eur. J. Pharm. Sci.* **151**, 105410 (2020).
36. J. Fu, W. Yu, X. Qian, Y. Wang, J. Ji, A photocatalytic carbon monoxide-generating effervescent microneedle patch for improved transdermal chemotherapy. *J. Mater. Chem. B* **11**, 5406–5415 (2023).
37. W. Yu, X. Li, Y. Huang, Y. Chen, Q. Gao, Y. Wang, J. Ji, Build an implanted "arsenal": Detachable microneedles for NIR-triggered cancer photothermo-chemotherapy. *Biomater. Sci.* **9**, 4737–4745 (2021).
38. A. Abramson, E. Caffarel-Salvador, V. Soares, D. Minahan, R. Y. Tian, X. Lu, D. Dellal, Y. Gao, S. Kim, J. Wainer, J. Collins, S. Tamang, A. Hayward, T. Yoshitake, H. C. Lee, J. Fujimoto, J. Fels, M. R. Frederiksen, U. Rahbek, N. Roxhed, R. Langer, G. Traverso, A luminal unfolding microneedle injector for oral delivery of macromolecules. *Nat. Med.* **25**, 1512–1518 (2019).
39. J. D. Byrne, M. N. R. Jajja, A. T. O'Neill, L. R. Bickford, A. W. Keeler, N. Hyder, K. Wagner, A. Deal, R. E. Little, R. A. Moffitt, C. Stack, M. Nelson, C. R. Brooks, W. Lee, J. C. Luft, M. E. Napier, D. Darr, C. K. Anders, R. Stack, J. E. Tepper, A. Z. Wang, W. C. Zamboni, J. J. Yeh, J. M. DeSimone, Local iontophoretic administration of cytotoxic therapies to solid tumors. *Sci. Transl. Med.* **7**, 273ra14 (2015).
40. F. Zhao, S. Fan, D. Ghate, S. Romanova, T. K. Bronich, S. Zhao, A hydrogel ionic circuit based high-intensity iontophoresis device for intraocular macromolecule and nanoparticle delivery. *Adv. Mater.* **34**, e2107315 (2022).
41. K. Moussi, A. A. Haneef, R. A. Alsiary, E. M. Diallo, M. A. Boone, H. Abu-Araki, O. O. Al-Radi, J. Kosel, A microneedles balloon catheter for endovascular drug delivery. *Adv. Mater. Technol.* **6**, 2100037 (2021).
42. H. L. Qian, S. Y. Chen, F. Jia, W. P. Huang, J. Wang, K. F. Ren, G. S. Fu, J. Ji, "Spongy skin" as a robust strategy to deliver 4-octyl itaconate for conducting dual-regulation against in-stent restenosis. *Biomaterials* **296**, 122069 (2023).
43. J. Wang, H. L. Qian, S. Y. Chen, W. P. Huang, D. N. Huang, H. Y. Hao, K. F. Ren, Y. B. Wang, G. S. Fu, J. Ji, miR-22 eluting cardiovascular stent based on a self-healable spongy coating inhibits in-stent restenosis. *Bioact. Mater.* **6**, 4686–4696 (2021).
44. J. Wang, Y. Xue, J. Liu, M. Hu, H. Zhang, K. Ren, Y. Wang, J. Ji, Hierarchical capillary coating to biofunctionlize drug-eluting stent for improving endothelium regeneration. *Research* **2020**, 1458090 (2020).
45. J. Wang, X.-C. Chen, Y.-F. Xue, M. Hu, Y.-B. Wang, K.-F. Ren, J. Ji, Thermo-triggered ultrafast self-healing of microporous coating for on-demand encapsulation of biomacromolecules. *Biomaterials* **192**, 15–25 (2019).
46. H. Y. Kim, J. H. Park, J.-H. Byun, J. H. Lee, S. H. Oh, BMP-2-immobilized porous matrix with leaf-stacked structure as a bioactive GBR membrane. *ACS Appl. Mater. Interfaces* **10**, 30115–30124 (2018).
47. D. Lin, Y. Chai, Y. Ma, B. Duan, Y. Yuan, C. Liu, Rapid initiation of guided bone regeneration driven by spatiotemporal delivery of IL-8 and BMP-2 from hierarchical MBG-based scaffold. *Biomaterials* **196**, 122–137 (2019).
48. H.-L. Qian, W.-P. Huang, Y. Fang, L.-Y. Zou, W.-J. Yu, J. Wang, K.-F. Ren, Z.-K. Xu, J. Ji, Fabrication of "spongy skin" on diversified materials based on surface swelling non-solvent-induced phase separation. *ACS Appl. Mater. Interfaces* **13**, 57000–57008 (2021).
49. X.-c. Chen, K.-f. Ren, W.-x. Lei, J.-h. Zhang, M. C. L. Martins, M. A. Barbosa, J. Ji, Self-healing spongy coating for drug "cocktail" delivery. *ACS Appl. Mater. Interfaces* **8**, 4309–4313 (2016).
50. H. Wu, D. K. Schwartz, Nanoparticle tracking to probe transport in porous media. *Acc. Chem. Res.* **53**, 2130–2139 (2020).
51. D. Kang, S. Kim, Y. Jeong, Exploring new avenues for de novo coronary artery disease: Next steps forward with drug-coated balloons. *JACC Asia* **4**, 532–535 (2024).
52. M. Yu, Y.-F. Yuan, F. Yang, J.-H. Xu, M.-L. Liu, S.-F. Nie, Y.-Y. Xiong, P. Libby, X. Cheng, Residual inflammatory risk in outcomes of chinese patients after percutaneous coronary intervention. *JACC Asia* **4**, 636–638 (2024).
53. J. Jin, F. Fang, W. Gao, H. Chen, J. Wen, X. Wen, J. Chen, The structure and function of the glycocalyx and its connection with blood-brain barrier. *Front. Cell. Neurosci.* **15**, 739699 (2021).
54. J. T. Tamsma, H. J. Keizer, A. E. Meinders, Pathogenesis of malignant ascites: Starling's law of capillary hemodynamics revisited. *Ann. Oncol.* **12**, 1353–1357 (2001).
55. A. T. Chwang, A. T. Chan, Interaction between porous media and wave motion. *Annu. Rev. Fluid Mech.* **30**, 53–84 (1998).
56. E. Latorre, S. Kale, L. Casares, M. Gómez-González, M. Uroz, L. Valon, R. V. Nair, E. Garreta, N. Montserrat, A. del Campo, B. Ladoux, M. Arroyo, X. Trepat, Active superelasticity in three-dimensional epithelia of controlled shape. *Nature* **563**, 203–208 (2018).
57. Y. Rao, S. Qiao, Z. Dai, N. Lu, Elastic wetting: Substrate-supported droplets confined by soft elastic membranes. *J. Mech. Phys. Solids* **151**, 104399 (2021).
58. X. Lu, J. Yang, J. B. Zhao, H. Gregersen, G. S. Kassab, Shear modulus of porcine coronary artery: Contributions of media and adventitia. *Am. J. Physiol. Heart Circ. Physiol.* **285**, H1966–H1975 (2003).
59. Q. Wang, Q. Liang, J. Dou, H. Zhou, C. Zeng, H. Pan, Y. Shen, Q. Li, Y. Liu, D. T. Leong, W. Jiang, Y. Wang, Breaking through the basement membrane barrier to improve nanotherapeutic delivery to tumors. *Nat. Nanotechnol.* **19**, 95–105 (2024).
60. D. Sun, J. Zhao, D. Liao, P. Chen, H. Gregersen, Shear modulus of the partially obstructed rat small intestine. *Ann. Biomed. Eng.* **45**, 1069–1082 (2017).
61. R. A. Byrne, M. Joner, F. Alfonso, A. Kastrati, Drug-coated balloon therapy in coronary and peripheral artery disease. *Nat. Rev. Cardiol.* **11**, 13–23 (2014).
62. S. X. Deng, J. Tomioka, J. C. Debes, Y. C. Fung, New experiments on shear modulus of elasticity of arteries. *Am. J. Physiol. Heart Circ. Physiol.* **266**, 1–10 (1994).
63. C. J. Greel, M. A. Lovich, E. R. Edelman, Arterial paclitaxel distribution and deposition. *Circ. Res.* **86**, 879–884 (2000).
64. A. R. Tzafriri, E. R. Edelman, "Convective and diffusive transport in drug delivery" in *Cancer Targeted Drug Delivery* (Springer, 2013), pp. 573–606.
65. E. L. Mills, D. G. Ryan, H. A. Prag, D. Dikovskaya, D. Menon, Z. Zaslona, M. P. Jedrychowski, A. S. H. Costa, M. Higgins, E. Hams, J. Szpyt, M. C. Runtsch, M. S. King, J. F. McGouran, R. Fischer, B. M. Kessler, A. F. McGettrick, M. M. Hughes, R. G. Carroll, L. M. Booty, E. V. Knatko, P. J. Meakin, M. L. J. Ashford, L. K. Modis, G. Brunori, D. C. Sevin, P. G. Fallon, S. T. Caldwell, E. R. S. Kunji, E. T. Chouchani, C. Frezza, A. T. Dinkova-Kostova, R. C. Hartley, M. P. Murphy, L. A. O'Neill, Itaconate is an anti-inflammatory metabolite that activates Nrf2 via alkylation of KEAP1. *Nature* **556**, 113–117 (2018).

66. G. L. Basatemur, H. F. Jørgensen, M. C. H. Clarke, M. R. Bennett, Z. Mallat, Vascular smooth muscle cells in atherosclerosis. *Nat. Rev. Cardiol.* **16**, 727–744 (2019).
67. T. Liu, Z. Liu, A. Jagota, C.-Y. Hui, Droplets on an elastic membrane: Configurational energy balance and modified Young equation. *J. Mech. Phys. Solids* **138**, 103902 (2020).

Acknowledgments: We thank J. Chen, Q. Huang, Y. Yu, and C. Zhang from the core facility platform of Zhejiang University School of Medicine for the technical support. **Funding:** This research was supported by the National Key Research and Development Program of China (2022YFB3807300), the National Natural Science Foundation of China (U20A20262, 51933009, and 52203190), the "Leading Goose" R&D Program of Zhejiang Province (2024C03052), and the Zhejiang Provincial Natural Science Foundation of China (LD22E030002). **Author contributions:** Conceptualization: H.Q., J.W., and J.J. Methodology: H.Q., J.W., Y.G., K.L., K.R., and J.J. Software: K.L. and Z.D. Validation: H.Q., J.W., Y.G., X.L., M.H., Y.Y., and K.R. Formal analysis: H.Q., J.W., Z.D., K.L., M.H., Y.Y., Y.L., and J.J. Investigation: H.Q., Y.G., X.L., M.H., Y.Y., and J.W. Resources: K.R. and J.J. Data curation: J.W. Writing—original draft: H.Q., J.W., and Z.D. Writing—review and editing: H.Q., J.W., K.L., and J.J. Visualization: H.Q., Y.G., J.W., and J.J. Supervision: J.W. and J.J. Project administration: J.W. and J.J. Funding acquisition: J.W. and J.J. **Competing interests:** The authors declare that they have no competing interests. **Data and materials availability:** All data needed to evaluate the conclusions in the paper are present in the paper and/or the Supplementary Materials.

Submitted 5 December 2024
Accepted 4 June 2025
Published 9 July 2025
10.1126/sciadv.adv1182